Research Article | Vol. 25, No. 21 | 16 Oct 2017 | OPTICS EXPRESS 25853
Optics EXPRESS

Low coherence digital holography microscopy based on the Lorenz-Mie scattering model

STIJN VANDEWIELE,[1,2,*] FILIP STRUBBE,[1,2] CASPAR SCHREUER,[1,2] KRISTIAAN NEYTS,[1,2] AND FILIP BEUNIS[1,2]

[1]*Ghent University, Liquid Crystals and Photonics Group, Department of Electronics and Information Systems, Technologiepark-Zwijnaarde 15, Ghent, 9052, Belgium*
[2]*Ghent University, Center for Nano- and Biophotonics, Ghent, Belgium*
[*]*stijn.vandewiele@ugent.be*

Abstract: We demonstrate the use of low spatial and temporal coherence holography microscopy, based on the Lorenz-Mie model, using the standard tungsten-halogen lamp present in an inverted microscope. An optical model is put forward to incorporate the effect of spectral width and different incidence angles of the incident light determined by the aperture at the back focal plane of the condenser lens. The model is validated for 899 nm diameter polystyrene microspheres in glycerol, giving a resolution of 0.4% for the index of refraction and 2.2% for the diameter of the particles.

OCIS codes: (090.1995) Digital holography; (110.2960) Image analysis; (290.4020) Mie theory.

References and links

1. F. Vollmer, S. Arnold, and D. Keng, "Single virus detection from the reactive shift of a whispering-gallery mode," Proc. Natl. Acad. Sci. U.S.A. **105**(52), 20701–20704 (2008).
2. S. Hosseini, F. Ibrahim, I. Djordjevic, H. A. Rothan, R. Yusof, C. van der Marel, A. Benzina, and L. H. Koole, "Synthesis and characterization of methacrylic microspheres for biomolecular recognition: Ultrasensitive biosensor for Dengue virus detection," Eur. Polym. J. **60**, 14–21 (2014).
3. T. Brans, F. Strubbe, C. Schreuer, K. Neyts, and F. Beunis, "Optical tweezing electrophoresis of single biotinylated colloidal particles for avidin concentration measurement," J. Appl. Phys. **117**, 214704 (2015).
4. X. Li, B. Zhang, W. Li, X. Lei, X. Fan, L. Tian, H. Zhang, and Q. Zhang, "Preparation and characterization of bovine serum albumin surface-imprinted thermosensitive magnetic polymer microsphere and its application for protein recognition," Biosens. Bioelectron. **51**, 261–267 (2014).
5. H. Chen, J. Kong, D. Yuan, and G. Fu, "Synthesis of surface molecularly imprinted nanoparticles for recognition of lysozyme using a metal coordination monomer," Biosens. Bioelectron. **53**, 5–11 (2014).
6. F. C. Cheong, B. Sun, R. Dreyfus, J. Amato-Grill, K. Xiao, L. Dixon, and D. G. Grier, "Flow visualization and flow cytometry with holographic video microscopy," Opt. Express **17**(15), 13071–13079 (2009).
7. F. Strubbe, S. Vandewiele, C. Schreuer, F. Beunis, O. Drobchak, T. Brans, and K. Neyts, "Characterizing and tracking individual colloidal particles using Fourier-Bessel image decomposition," Opt. Express **22**(20), 24635–24645 (2014).
8. O. M. Maragò, P. H. Jones, P. G. Gucciardi, G. Volpe, and A. C. Ferrari, "Optical trapping and manipulation of nanostructures," Nat. Nanotechnol. **8**(11), 807–819 (2013).
9. K. W. Allen, N. Farahi, Y. Li, N. I. Limberopoulos, D. E. Walker, Jr., A. M. Urbas, and V. N. Astratov, "Overcoming the diffraction limit of imaging nanoplasmonic arrays by microspheres and microfibers," Opt. Express **23**(19), 24484–24496 (2015).
10. M. Tassieri, F. Del Giudice, E. J. Robertson, N. Jain, B. Fries, R. Wilson, A. Glidle, F. Greco, P. A. Netti, P. L. Maffettone, T. Bicanic, and J. M. Cooper, "Microrheology with Optical Tweezers: Measuring the relative viscosity of solutions 'at a glance'," Sci. Rep. **5**, 8831 (2015).
11. T. Brans, F. Strubbe, C. Schreuer, S. Vandewiele, K. Neyts, and F. Beunis, "Joule heating monitoring in a microfluidic channel by observing the Brownian motion of an optically trapped microsphere," Electrophoresis **36**(17), 2102–2109 (2015).
12. J. Westerweel, "Fundamentals of digital particle image velocimetry," Meas. Sci. Technol. **8**, 1379 (1997).
13. C. Weis, C. Oelschlaeger, D. Dijkstra, M. Ranft, and N. Willenbacher, "Microstructure, local dynamics, and flow behavior of colloidal suspensions with weak attractive interactions," Sci. Rep. **6**, 33498 (2016).
14. F. Beunis, F. Strubbe, K. Neyts, and D. Petrov, "Beyond Millikan: the Dynamics of Charging Events on Individual Colloidal Particles," Phys. Rev. Lett. **108**(1), 016101 (2012).
15. I. Tavernier, W. Wijaya, P. Van der Meeren, K. Dewettinck, and A. R. Patel, "Food-grade particles for emulsion stabilization," Trends Food Sci. Technol. **50**, 159–174 (2016).

#305133 https://doi.org/10.1364/OE.25.025853
Journal © 2017 Received 22 Aug 2017; revised 26 Sep 2017; accepted 30 Sep 2017; published 10 Oct 2017

Optics EXPRESS

16. F. C. Cheong, K. Xiao, and D. G. Grier, "Technical note: Characterizing individual milk fat globules with holographic video microscopy," J. Dairy Sci. **92**(1), 95–99 (2009).
17. J. Bahtz, D. Z. Gunes, A. Syrbe, N. Mosca, P. Fischer, and E. J. Windhab, "Quantification of Spontaneous W/O Emulsification and its Impact on the Swelling Kinetics of Multiple W/O/W Emulsions," Langmuir **32**(23), 5787–5795 (2016).
18. B. J. Krishnatreya, A. Colen-Landy, P. Hasebe, B. A. Bell, J. R. Jones, A. Sunda-Meya, and D. G. Grier, "Measuring Boltzmann's constant through holographic video microscopy of a single colloidal sphere," Am. J. Phys. **82**, 23–31 (2013).
19. J. Fung, R. W. Perry, T. G. Dimiduk, and V. N. Manoharan, "Imaging multiple colloidal particles by fitting electromagnetic scattering solutions to digital holograms," J. Quant. Spectrosc. Radiat. Transf. **113**, 2482–2489 (2012).
20. A. Wang, T. G. Dimiduk, J. Fung, S. Razavi, I. Kretzschmar, K. Chaudhary, and V. N. Manoharan, "Using the discrete dipole approximation and holographic microscopy to measure rotational dynamics of non-spherical colloidal particles," J. Quant. Spectrosc. Radiat. Transf. **146**, 499–509 (2014).
21. A. Wang, R. F. Garmann, and V. N. Manoharan, "Tracking E. coli runs and tumbles with scattering solutions and digital holographic microscopy," Opt. Express **24**(21), 23719–23725 (2016).
22. F. Saglimbeni, S. Bianchi, G. Bolognesi, G. Paradossi, and R. Di Leonardo, "Optical characterization of an individual polymer-shelled microbubble structure via digital holography," Soft Matter **8**, 8822 (2012).
23. B. Schneider, J. Dambre, and P. Bienstman, "Fast particle characterization using digital holography and neural networks," Appl. Opt. **55**(1), 133–139 (2016).
24. F. C. Cheong, K. Xiao, D. J. Pine, and D. G. Grier, "Holographic characterization of individual colloidal spheres' porosities," Soft Matter **7**, 6816–6819 (2011).
25. C. Wang, X. Zhong, D. B. Ruffner, A. Stutt, L. A. Philips, M. D. Ward, and D. G. Grier, "Holographic Characterization of Protein Aggregates," J. Pharm. Sci. **105**(3), 1074–1085 (2016).
26. F. Dubois, L. Joannes, and J.-C. Legros, "Improved three-dimensional imaging with a digital holography microscope with a source of partial spatial coherence," Appl. Opt. **38**(34), 7085–7094 (1999).
27. P. Kolman and R. Chmelík, "Coherence-controlled holographic microscope," Opt. Express **18**(21), 21990–22003 (2010).
28. A. D. Ward, M. Zhang, and O. Hunt, "Broadband Mie scattering from optically levitated aerosol droplets using a white LED," Opt. Express **16**(21), 16390–16403 (2008).
29. G. Pedrini and S. Schedin, "Short coherence digital holography for 3D microscopy," Opt.-. Int. J. Light Electron Opt. **112**, 427–432 (2001).
30. J. A. Stratton and J. A. Stratton, "Boundary-Value Problems," in *Electromagnetic Theory* (John Wiley & Sons, Inc., 2015), pp. 482–599.
31. K. Kvien, "Angular spectrum representation of fields diffracted by spherical objects: physical properties and implementations of image field models," J. Opt. Soc. Am. A **15**, 636 (1998).
32. S.-H. Lee, Y. Roichman, G.-R. Yi, S.-H. Kim, S.-M. Yang, A. van Blaaderen, P. van Oostrum, and D. G. Grier, "Characterizing and tracking single colloidal particles with video holographic microscopy," Opt. Express **15**(26), 18275–18282 (2007).
33. Y. Zhu, B. Carragher, F. Mouche, and C. S. Potter, "Automatic particle detection through efficient hough transforms," IEEE Trans. Med. Imaging **22**(9), 1053–1062 (2003).
34. R. Parthasarathy, "Rapid, accurate particle tracking by calculation of radial symmetry centers," Nat. Methods **9**(7), 724–726 (2012).
35. B. J. Krishnatreya and D. G. Grier, "Fast feature identification for holographic tracking: the orientation alignment transform," Opt. Express **22**(11), 12773–12778 (2014).
36. X. Ma, J. Q. Lu, R. S. Brock, K. M. Jacobs, P. Yang, and X.-H. Hu, "Determination of complex refractive index of polystyrene microspheres from 370 to 1610 nm," Phys. Med. Biol. **48**(24), 4165–4172 (2003).
37. S. H. Jones, M. D. King, and A. D. Ward, "Determining the unique refractive index properties of solid polystyrene aerosol using broadband Mie scattering from optically trapped beads," Phys. Chem. Chem. Phys. **15**(47), 20735–20741 (2013).
38. L. A. Philips, D. B. Ruffner, F. C. Cheong, J. M. Blusewicz, P. Kasimbeg, B. Waisi, J. R. McCutcheon, and D. G. Grier, "Holographic characterization of contaminants in water: Differentiation of suspended particles in heterogeneous dispersions," Water Res. **122**, 431–439 (2017).

1. Introduction

Accurate and precise characterization of spherical colloidal particles is an important method in research fields such as biosensing [1–7], microscopy techniques [8–11], fluid flow tracing [12,13], the study of elektrokinetic effects with tracer particles [14] and food monitoring [15–17]. The size and refractive index of the colloidal particles are two properties often sought after as the first leads to information on the size distribution of the dispersion and the second gives insight in the composition and structural properties such as a coating or porosity.

In the last decade holographic video microscopy based on fitting the acquired particle images to simulated Lorenz-Mie scattering holograms has proven to allow accurate

Optics EXPRESS

characterization of single spherical particles with high resolving power. This microscope-compatible method is able to capture time-dependent information on the position of individual spheres in three dimensions, on the particle's diameter and on its refractive index. A resolution down to 1 nm in radius and less than 0.001 refractive index units (RIU) has been demonstrated for individual particles [18]. The potential to expand the technique to the fitting of more complex scattering theories has been validated for a multisphere model [19], the discrete dipole approximation [20,21] and core-shell particles [22,23].

The typical implementation uses a highly coherent laser beam as the illumination source. Forward scattered light from a particle interferes with the incident beam, leading to an interference pattern. Using a highly coherent and powerful laser beam allows to generate a near-planar incident light field over a large field of view, to obtain a high hologram contrast, and to use short exposure times to avoid blurring related to particle movement (e.g. due to Brownian motion or drift). The technique makes it possible to detect biochemical reactions on polymer bioprobes such as avidin-biotin reaction [6], to estimate the porosity of single particles [24], and to inspect the quality of milk [16] and protein aggregates [25].

Up to now the idea of using a low-coherence illumination source has not been investigated for Lorenz-Mie holographic video microscopy. It is known however that a partially coherent light source has advantages over a strongly coherent one, such as cancellation of coherence noise, avoiding overlap of long-ranging scatter patterns from multiple particles, and lower sensitivity to environmental changes or defects along the optical path. These factors may potentially limit the attainable resolving power and are associated to the high coherence length of the light source [26]. Another possible reason to opt for a partially coherent light source is an overall reduction in system cost.

These advantages were explored earlier in a video microscopy setup with Köhler illumination [7]. Here an image analysis method based on multiple image moments was used to analyze images of light scattered by micrometer-sized plastic spheres with different radii and composition. The method achieves a resolution of 0.4% in refractive index and 1% in size. However, the method relies on the availability of calibration standards, because no optical modeling is involved.

A partially coherent light source typically diminishes or completely cancels coherence noise, at the cost of reducing the theoretically attainable resolving power [26,27]. The use of a low-coherence illumination method has already demonstrated its potential to probe the size and refractive index of micrometer sized colloidal particles [28], and as a general holographic microscopy method [27,29].

In this article we investigate the use of a low-coherent light source for in-line Lorenz-Mie holography. We use the standard tungsten-halogen lamp present in an inverted Nikon Ti-Eclipse microscope as a non-coherent light source and make it partially coherent by using a combination of an aperture at the back focal plane of the condenser and a narrow bandpass color filter. The necessary adjustments to the theory and the effect of partial coherence are described. Additionally, we describe a center detection method that can cope with a large range of noise levels. Decoupling the center detection from the 2D image hologram fitting results in a substantial computational performance gain, which can be realized by matching the noise-filtered radial profile to the theoretical Lorenz-Mie scattering profile.

The method is validated in two ways. Firstly the correlation between the resulting diameter or refractive index and the fitted z-position of the particle is determined. Thereafter the method is tested to verify if the particle's properties correspond to the values provided by the manufacturer.

2. Materials

The test sample consists of a dispersion of polystyrene microspheres from Polysciences having a narrow size distribution. The batch was certified (NIST traceable) having a mean diameter of 899.0 ± 11.3 nm and a standard deviation of 31 nm. The microspheres are

Optics EXPRESS

dispersed in glycerol with 0.02 wt% Tween20 to stabilize the dispersion. By diluting the suspension to a degree where on average only one particle is present in the volume of view (80 µm x 80 µm x 90 µm for a 100x objective) it is possible to avoid overlap of scatter patterns.

The sample is loaded by capillary means in a microfluidic channel. These microfluidic devices are fabricated with a #1 microscope cover glass and a microscope slide. These are first thoroughly cleaned by consecutively rinsing them in an ultrasonic bath with an RBS solution in DI water for 15 minutes, in pure DI water for 15 minutes, blown dry with nitrogen air, in acetone for 15 minutes, in isopropanol for 15 minutes, in DI water for 15 minutes and finally blown dry with nitrogen air. The channel side walls are fabricated using a DispenseMate glue plotter dispensing a dispersion of 90 µm diameter silica microspheres (MO-SCI Speciality Products, LLC) in Norland Optical Adhesive 68 UV-curable glue. After bringing the slides together the glue is cured with UV light.

3. Optical setup

The experiments are conducted using a Nikon Ti Eclipse inverted microscope, schematically depicted in Fig. 1. The standard 100 W tungsten-halogen lamp serves as the illumination source. A diffuser, placed between the field diaphragm and the lamp, eliminates spatial variations in brightness over the sample plane. To impose a certain degree of spectral coherence a color filter (excitation filter of the Nikon G-2A filter cube, having a bandpass characteristic from 510 to 560 nm) is placed behind the diffuser to select the desired spectral coherence. Additionally, an aperture (1000 µm diameter) is placed at the back focal plane of the condenser lens (a 1 inch diameter Thorlabs achromatic doublet with 30 mm focal distance) to increase the spatial coherence. The incident and scattered light are collected using a high numerical aperture, high magnification objective (Nikon CFI Plan Fluor 100X oil immersion objective with NA = 1.3) and imaged on an Andor iXon DU885 EMCCD camera.

The alignment of optical components is as follows. The distance between the aperture and the condenser lens is set so that a collimated beam is obtained, i.e. a sharp image of the aperture forms at infinity. Practically this is achieved by forming a sharp image of the aperture on a wall 5 m away from the microscope. To allow for tilt correction of the incident beam with respect to the optical axis the aperture is placed on an XY-stage. When the sample is loaded and the objective is focused at the desired focal plane, the complete condenser system is translated along the optical axis until the field diaphragm is in focus and Köhler illumination is obtained.

During experiments the field diaphragm is matched with the field of view on the camera to reduce the collection of light scattered by particles outside of the field of view. Additionally the exposure time (33 ms) was set to enable the maximum full frame rate while the EMCCD gain setting was chosen so that the intensity histogram of the full image is centered on the 14 bit dynamic range of the camera enabling maximum image intensity resolution without saturation.

Optics EXPRESS

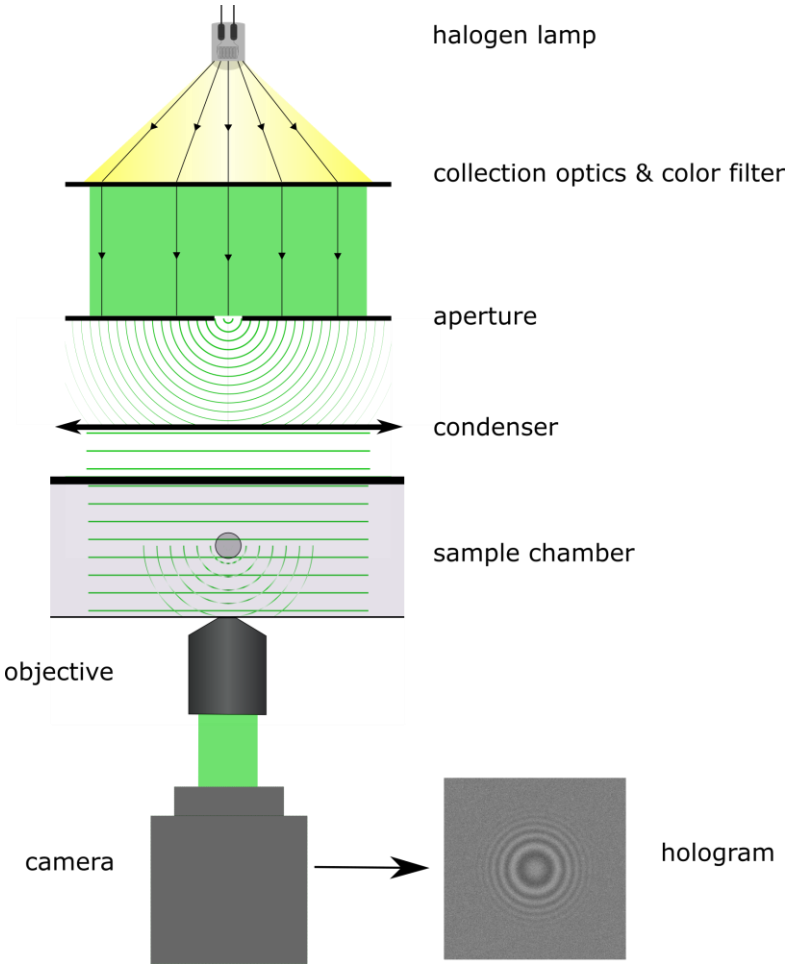

Fig. 1. Schematic drawing of the setup for incoherent holography microscopy.

4. Optical simulation model for the hologram

The standard Lorenz-Mie scattering model that is commonly used for holographic video microscopy, assumes a linearly polarized and monochromatic plane wave, incident on a spherical particle with diameter D_p and refractive index n_p in an isotropic and uniform medium with refractive index n_m [30]. The normalized hologram generated by the interference of a plane wave, travelling along the optical axis z and, linearly polarized along the $\bar{1}_i$ direction, with the scattered field $\overline{E}_{s,i}$ from a spherical particle centered at the origin (z = 0), expressed in cylindrical coordinates is given by

$$I_k(\rho,\varphi,z) = \left| e^{ikz}\bar{1}_i + \overline{E}_{s,i} \right|^2 \tag{1}$$

or

$$I_k(\rho,\varphi,z) = 1 + 2\Re\mathrm{e}\left\{ e^{ikz}\bar{1}_i \overline{E}^*_{s,i} \right\} + |\,\overline{E}_{s,i}\,|^2 \tag{2}$$

with ρ the radial position in the focal plane, φ the polar angle in the focal plane and z the distance of the focal plane to the particle. The second term is the coherence term and the third term is the intensity of the scattered field.

Optics EXPRESS

For the microscope setup described above, the basic formula given here does not suffice. First of all, the incident light is not or only partially polarized. Additionally, the light is not monochromatic but has a certain spectral width. Finally, the incident light is not a plane wave but has a limited degree of spatial coherence determined by the finite aperture at the back focal plane of the condenser. These differences are addressed and incorporated in the theory presented below in order to simulate the hologram resulting from spherical particles in the microscope setup.

For a well-aligned microscope the camera and the focal plane are in conjugate planes. The hologram detected at the camera is the same hologram evaluated on the focal plane, apart from a magnification factor determined by the microscope setup.

4.1 Unpolarized light

As stated, Eqs. (1) and (2) hold for linearly polarized light. For light arbitrary polarized in the plane perpendicular to the optical axis the hologram profile can be described as

$$I_k(\rho,\varphi,z)=\left|p_x\left(e^{ikz}\bar{1}_x+\overline{E}_{s,x}\right)+p_y\left(e^{ikz}\bar{1}_y+\overline{E}_{s,y}\right)\right|^2 \tag{3}$$

Where p_x and p_y are complex values defining the polarization state and $|p_x|^2+|p_y|^2=1$, $x=\rho\cos(\varphi)$ and $y=\rho\sin(\varphi)$. With incoherent, unpolarized light there is no fixed relationship between p_x and p_y over time. The cross product will therefore vanish leading to

$$I_k(\rho,\varphi,z)=\left|p_x\left(e^{ikz}\bar{1}_x+\overline{E}_{s,x}\right)\right|^2+\left|p_y\left(e^{ikz}\bar{1}_y+\overline{E}_{s,y}\right)\right|^2 \tag{4}$$

Averaging this profile around the azimuthal angle φ and taking into account that the φ-averaged profiles for the *x*-polarization and *y*-polarization are indistinguishable, results in the radial profile given by

$$I_k(\rho,z)=1+\Re\mathrm{e}\left\{e^{ikz}\bar{1}_i\,\overline{E}^*_{s,i}(\rho,z)\right\}+\frac{1}{2}|\,\overline{E}_{s,i}(\rho,z)\,|^2 \tag{5}$$

The factor ½ in the coherence and intensity term originates from the averaging of $\cos^2\varphi$ and $\sin^2\varphi$ in the vector terms. $\overline{E}_{s,i}(\rho,z)$ is the scattered electric field $\overline{E}_{s,i}(\rho,\varphi,z)$ where the azimuthal part is discarded.

The radial profile as seen in the focal plane at a distance of 15 µm away from the particle for φ = 0° and 90° for linearly polarized light along the y-axis (φ = 90°) is shown in Fig. 2 as a function of the scattering angle θ with $\tan(\theta)=\rho/z$. These clearly distinctive profiles demonstrate that the polarization state of the incident light should be known a priori or fitted when analyzing full 2D holograms stemming from polarized light. Not taking this into account leads to inaccuracies during the analysis of hologram images. Analysis of the azimuthal averaged radial profiles does not require knowledge of the polarization state of the incident light, resulting in an advantage over the analysis of full 2D holograms.

Optics EXPRESS

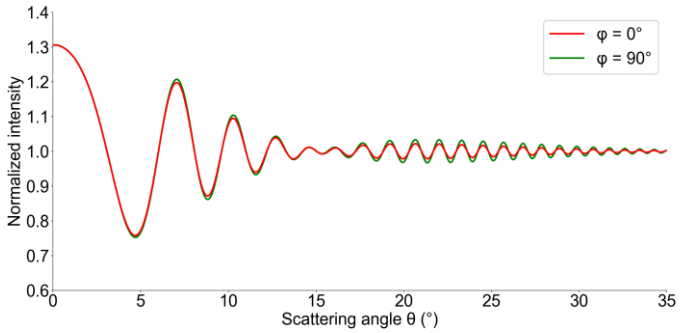

Fig. 2. Simulated radial intensity profile for a 899 nm PS particle in glycerol, illuminated with a plane wave (λ = 500 nm), for incident light that is linearly polarized along the x-axis. The profiles are taken for φ = 0° and 90° for z = 10 µm.

4.2 Effect of spectral width

The finite spectral range is addressed by incoherently integrating the resulting holograms for every wavenumber k in the incident field, weighted by the relative spectral density $w_k(k)$ of the incident light, within the spectral range $[k_1, k_2]$:

$$I_{\Delta k}(\rho, z) = \int_{k_1}^{k_2} I_k(\rho, z) w_k(k) dk \tag{6}$$

Numerically, (6) can be computed efficiently and accurately by using a Gauss-Legendre quadrature.

Figure 3 illustrates the effect of spectral width for a constant spectral density, on the simulated scatter pattern for a particle dispersed in water at a distance of z = 15 µm above the focal plane. The incident light consists of a superposition of plane waves along the z-axis with different frequencies.

With increasing spectral width, we observe an angle-dependent decrease in contrast while the position of the minima/maxima peaks remains the same. Only for large $\Delta\lambda$ or large scattering angles these peaks start to shift.

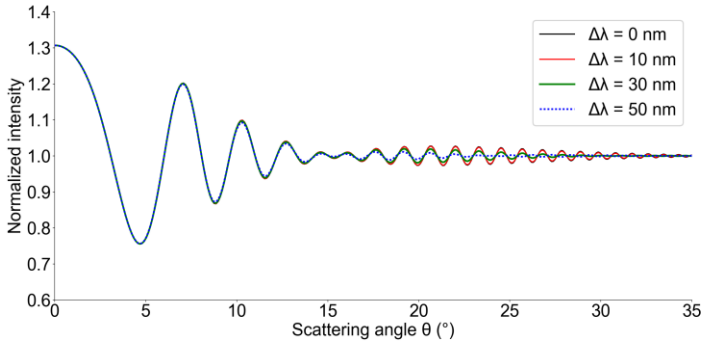

Fig. 3. Effect of spectral width on the simulated polarization-averaged radial profile of the hologram for a 899 nm PS particle dispersed in glycerol at a distance of z = 10 µm above the focal plane. The spectral widths are $\Delta\lambda$ = 10 nm, 30 nm and 50 nm around a central wavenumber 1/500 nm^{-1}.

Optics EXPRESS

4.3 Effect of a finite aperture size

We use in our setup the tungsten halogen lamp standardly present in the microscope, which we assume to emit completely incoherent light. This allows us to treat the effect of a finite aperture size similarly as we did for the finite spectral range, i.e. by integrating the resulting holograms for every wave vector $\bar{k}$ in the incident field. Every point within the aperture is assumed to result in an illuminating plane wave (see Fig. 4(a)) with an inclination. The maximum inclination angle δ is defined by the diameter d of the aperture and the focal distance f of the condenser lens.

$$\tan(\delta_{air}) = \frac{d}{2f} \tag{7}$$

While the incident light is generated in air, the scattering field is generated in the liquid medium. A correction to obtain the polar angle δ_m of the incident field in the medium is required, according to Snell's law.

$$\sin(\delta_{air}) = n_m \sin(\delta_m) \tag{8}$$

The measurements were performed using an aperture with a diameter of 1000 µm, corresponding to a maximum illumination angle in air of 0.95° for a focal distance of 30 mm.

Because the aperture is small, the hologram resulting from a point in the aperture at a distance σ from the center is in good approximation given by the hologram from the central point that is shifted over a distance $\sigma z / f$ in the radial direction ρ. To obtain the hologram for the full aperture, we have to average the holograms that are shifted over a disc with radius $\Delta = z\tan(\delta_m)$ as shown in Fig. 4(b). By inserting (7) and (8) and making use of the small-angle approximation $\sin(\delta_m) \approx \tan(\delta_m)$ we obtain $\Delta = \frac{zd}{2n_m f}$. The resulting intensity for the radial profile is given by:

$$I_a(\rho, z) = \frac{1}{\pi\Delta^2}\int_0^{2\pi}\int_0^{\Delta} I_{\Delta k}(\rho', z)\, s\, ds\, d\varphi \tag{9}$$

Where ρ' is the radial coordinate in the shifted hologram. This can be related to the radial coordinate ρ in the original hologram:

$$\begin{aligned} \rho' &= \sqrt{x'^2 + y'^2} \\ &= \sqrt{(x+s)^2 + y^2} \\ &= \sqrt{(\rho\cos(\varphi)+s)^2 + (\rho\sin(\varphi))^2} \\ &= \sqrt{\rho^2 + s^2 + 2s\rho\cos\varphi} \end{aligned} \tag{10}$$

Here, we have chosen to make the displacement only along the x-axis. Due to angular symmetry in the hologram the resulting angularly averaged profile for a hologram shifted over a distance s will be identical for every direction the shift is performed in.

This finally leads to

$$I_a(\rho, z) = \frac{1}{\pi\Delta^2}\int_0^{2\pi}\int_0^{\Delta} I_{\Delta k}(\sqrt{\rho^2 + s^2 + 2s\rho\cos\varphi}, z)\, s\, ds\, d\varphi \tag{11}$$

Inserting (6) for the spectral range leads to

Optics EXPRESS

$$I_{sim}(\rho,z)=\frac{1}{\pi\Delta^2}\int_0^{2\pi}\int_0^{\Delta}\int_{k_1}^{k_2} I_k(\sqrt{\rho^2+s^2+2s\rho\cos\varphi},z)w_k(k)dksdsd\varphi \qquad (12)$$

with $I_k(\rho,z)$ given by (5) which can be calculated with the standard equations for Lorenz-Mie theory [30].

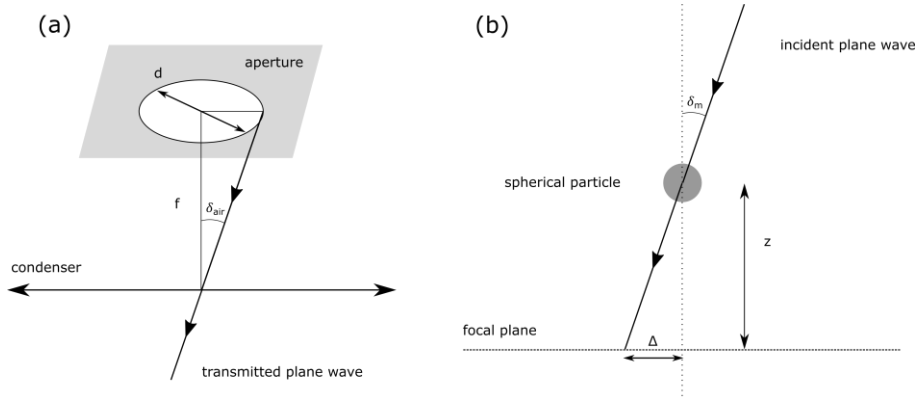

Fig. 4. (a) Schematic of the incident light on an aperture with diameter *d*. (b) Schematic representation of a spherical particle illuminated under an angle.

How well this approximation holds is illustrated in Fig. 5(a), showing the comparison between the approximation and the exact simulation for different values of an aperture as defined through δ_{air}. The approximation and the exact solution match well, but starts to fail at larger scattering angles θ and larger illumination angles δ_{air}. The phase of the scattered field can even be off by π as can be seen in Fig. 5(b) for δ = 2.0° and θ > 20° where the approximation shows minima in intensity while the exact solution gives maxima. For δ = 1.0° the phase is off by π starting at θ ≈35° (not shown on the figure). The scattering angle for which the phase is off by π thus shifts to lower values with an increasing value for δ.

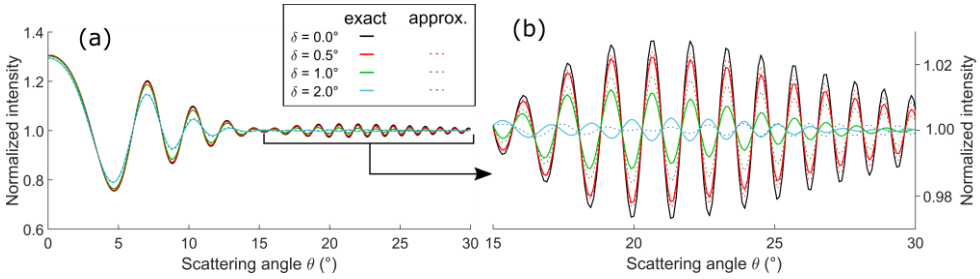

Fig. 5. (a) Effect of illumination aperture as defined by δ_{air} on the simulated radial profile for a 899 nm diameter PS particle in glycerol, illuminated with a single wavelength λ = 500 nm. Both the exact simulation and the approximation are shown. Focal plane at *z* = 10 µm. (b) Zoom on the region for larger scattering angles θ between 15° and 30°.

5. Image analysis and the fitting method

The final goal of the fitting method is to match the experimentally obtained radial profile $I_{\text{norm}}(\rho)$ of the hologram with the simulated one $I_{\text{sim}}(\rho)$ by minimizing the error

$$err=\int_0^{R_{crop}}\left(I_{\text{norm}}(\rho)-I_{\text{sim}}(\rho)\right)^2\rho d\rho \qquad (13)$$

where ρ is the radial coordinate and R_{crop} determines the cropping window for analysis.

Optics EXPRESS

In the first step the experimental image with the lamp ON is normalized by the background by

$$I_{\text{norm}}(x,y) = \beta \frac{I_{\text{experiment}}(x,y)}{I_{\text{background}}(x,y)} \tag{14}$$

The background image is preferentially obtained at the same *xyz* center position of the focal plane to eliminate the scattering of all nearby structures. For a freely diffusing particle this can be done by computing the median value for each pixel of all frames of the experiment. For the case where the objective is scanned along the optical axis, a second scan can be performed at a different *xy* position, free of scattering objects in the field of view. The fitting parameter β serves to compensate for possible intensity fluctuations of the incident light field and is fitted during minimization of the error in (13).

In contrast to the method in [31] where the full 2D image is used during fitting to a simulated hologram, our fitting method uses the radially averaged profile. Working with only the radial profile has advantages in computational speed and acts as a noise-filter. The particle's center position (x_c, y_c) must be known prior to this fit, however. Different algorithms exist for the center detection of particle images including the center of mass, Hough transform and voting [32], or center of symmetry transform. This last method outperforms the other mentioned methods in accuracy [33,34].

Direct implementation of the methods in [33,34] is not feasible as the images acquired through our method suffer from a high level of noise since a small aperture is used and only a small fraction of the light from the lamp reaches the camera. This high noise level makes the calculation of an image gradient cumbersome without heavy application of noise filtering algorithms. We can alternatively find the particle's center by directly searching for the center of symmetry, weighted by the angular averaged contrast. This makes the intermediate step of image gradient calculation obsolete.

The used center detection algorithm works by maximizing a functional corresponding to the maximum contrast and center of symmetry using a Nelder-Mead optimization algorithm.

$$contrast = \frac{\int \left(\int I_{\text{norm}}\left(x_c + \rho\cos\theta, y_c + \rho\sin\theta\right) d\theta - 1 \right)^2 \rho d\rho}{\iint \left(I_{\text{norm}}\left(x_c + \rho\cos\theta, y_c + \rho\sin\theta\right) - I_{\text{norm}}\left(x_c - \rho\cos\theta, y_c - \rho\sin\theta\right) \right)^2 \rho d\rho d\theta} \tag{15}$$

The nominator calculates the contrast for a center candidate (x_c, y_c) with respect to the background value equal to 1. This contrast is weighted by a value proportional to the angular symmetry of the pattern, taking into account possible anisotropy due to (partial) polarization.

The calculation of the contrast indirectly relies on the value of β through I_{norm}. Because β is only known after fitting the image we can use the value of β from the previous frame. This is justified as it has only a minor effect on the center detection. It mainly serves to prevent the optimization algorithm from converging to an area without particle.

The schematic workflow is illustrated for an experimental obtained image in Fig. 6.

Optics EXPRESS

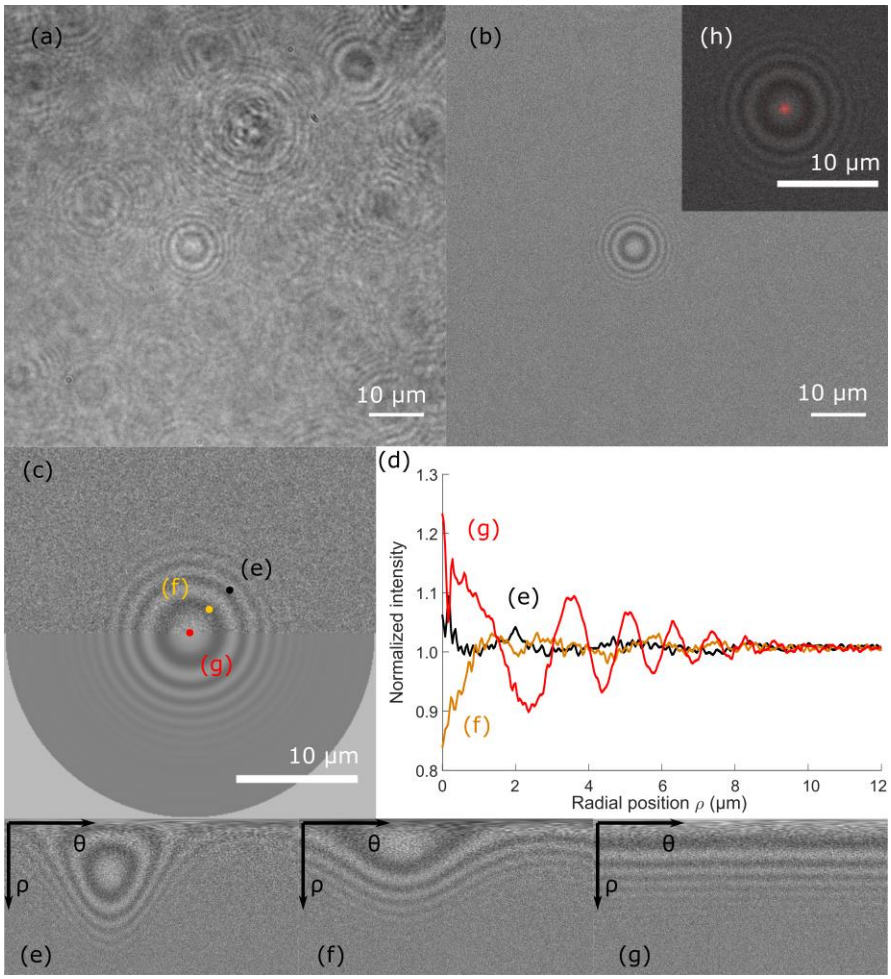

Fig. 6. Example of the center detection method for a 899 nm diameter PS particle in glycerol illuminated with the G-2A colour filter and made use of an aperture with diameter of 1000 µm. (a) The full frame (1004 x 1002 pixels) raw image $I_{\text{experiment}}(x, y)$ as acquired by the camera. Each pixel corresponds to 80 nm x 80 nm in the object plane. (b) Background normalized image $I_{\text{norm}}(x, y)$. (c) The top part shows the centered background normalized image, the bottom part shows the centered noise reduced radial profile expanded to a 2D image. (d) The averaged radial profiles $I_{\text{norm}}(\rho)$ for the three different positions marked in (c). (e)-(g) Polar plot of the intensity for the three different center position candidates marked in (c). (h) Shows a plot of the weighted contrast (red) in the vicinity of the particle's center. The scalebar in (a), (b), (c) and (h) corresponds to 10 µm.

When the particle center is located the radius, refractive index, z-position and β are fitted by using a Levenberg-Marquandt minimization algorithm on (13) to find the best fit.

Since the theoretical model is most suitable for smaller scattering angles and smaller illumination angles, the radial profile is cut off at a (half)-scattering angle of θ_{crop} = 20°. This also reduces the required computing time during fitting. The relationship between this angle and the radius R_{crop} on the camera, with M the magnification in use in the microscope, is given by

$$R_{crop} = \frac{z}{M}\tan\left(\theta_{crop}\right) \tag{16}$$

Optics EXPRESS

The distance between the particle and the focal plane z is not known a priori and is one of the fitting parameters. We can make use of the fitting result of the previous frame and use this value as an approximation, however.

6. Results and discussion

6.1 Influence of corrections

To study the influence of the corrections made to the optical model for the calculation of the scattering hologram the analysis of a video is presented here with the various corrections applied or not. Only data for $|z| > 5$ µm is shown.

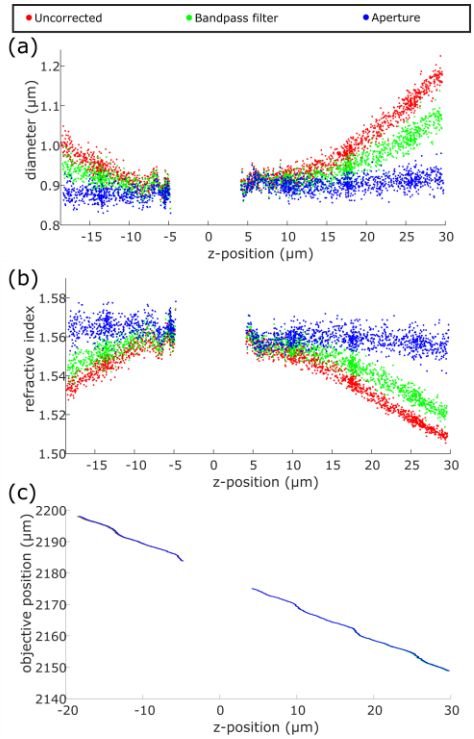

Fig. 7. Effect on the fitted diameter, refractive index and z-position for the different successive corrections present in the optical model. (a) The fitted diameter as a function of the fitted z-position. (b) The fitted refractive index as a function of the fitted z-position. (c) The fitted z-position over time with respect to the focal plane.

As can be seen from Fig. 7, the model adaptations lower the correlation between the obtained refractive index or diameter and the obtained z-position of the particle. This validates the optical model for taking most of the z-dependent effects into account.

Additionally, the obtained z-position is almost independent of the effects we have corrected for. Holographic video microscopy based on fitting of Lorenz-Mie scattering profiles can thus be considered a very powerful tool to track spherical particles in 3D.

Comparison between the experimentally found radial profile, the fit and the nominally expected values are shown in Fig. 8 for a single frame around z = 5 µm and z = 15 µm. Although only the part where $\theta < 20°$ was used during fitting, the correspondence between the experimental data and the fit are also good at larger scattering angles for z = 15 µm. This is not the case for z = 5 µm, where a discrepancy can be found for larger angles.

The expected curve, obtained by simulating a hologram formed for a particle with size given by the manufacturer and a refractive index as found in literature, shows a higher

Optics EXPRESS

contrast than measured (approximately 26% and 30% at the forward scattering angle θ = 0° for respectively z = 15 µm and z = 5 µm). This results in a fit where the measured refractive index is lower than that found in literature for bulk material. The particle's size is within the constraints of the specifications as given by the manufacturer, however.

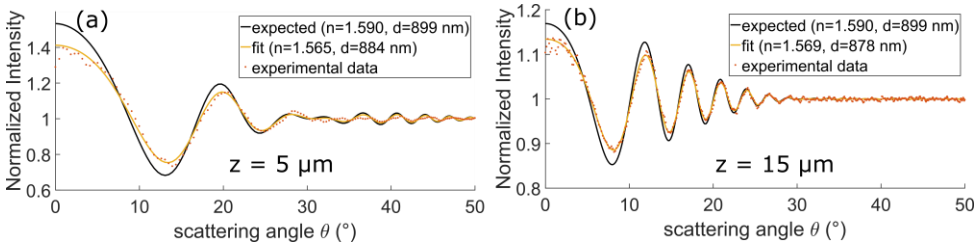

Fig. 8. Simulated, fitted and nominally expected radial intensity profile from a single frame for a particle in glycerol at two different z-positions. During the fit only data corresponding to θ < 20° was used. (a) z = 5 µm. (b) z = 15 µm

6.2 Particles in glycerol

To reduce the refractive index mismatch between the immersion liquid of the objective, the glass slide and the dispersion medium, the polystyrene particles were dispersed in glycerol having a refractive index of 1.47, close to that of glass (n_{glass} = 1.515). Because of its high viscosity (1400x that of water at room temperature) Brownian motion of the particles is drastically reduced. To obtain a *z*-scan of a particle the objective (and thus the focal plane) was moved over a range of 60 µm (in steps of 25 nm). An exact background could therefore not be obtained, but was created by performing the same z-scan at a nearby *xy*-position in the absence of any particles.

For small distances to the focal plane the fit results in questionable fitting values. Therefore we've cleaned up the data based on the fitting result of β. Frames for which β deviates more than 0.5% from the found nominal value were discarded.

A histogram together with the mean and standard deviation of the refractive index and diameter is shown per particle in Fig. 9. The values for the diameter are consistent with that specified by the manufacturer. The refractive index is systematically lower (around 1.57) than that previously found for polystyrene microspheres (1.59-1.60) [35,36]. As was coined before in [24] polystyrene particles may possess some degree of porosity depending on the fabrication parameters.

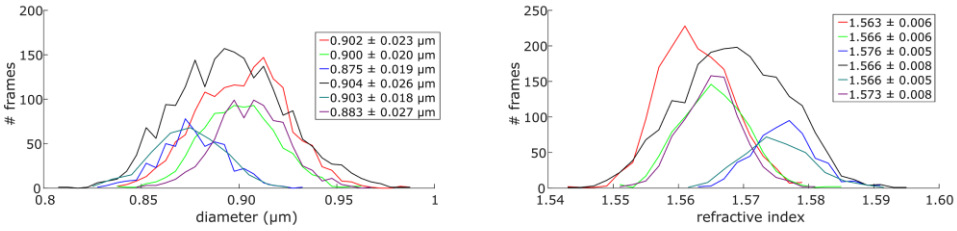

Fig. 9. Histogram of the measured diameter and refractive index for the six individual particles over the complete *z*-range. Identical colors in the two histograms correspond to the same particle.

The results show a resolution around 20 nm or 2.2% for the diameter and 0.006 or 0.4% in absolute value for the refractive index (6% relative to the difference between the RI of the particle and that of the medium). These values are similar as those obtained in our previous size and refractive index analysis method as described in [37,38] with the added advantage that it does not rely on calibration standards.

Optics EXPRESS

7. Conclusion and outlook

We have demonstrated a working low-coherence holographic characterization tool for spherical polystyrene particles in glycerol. The optical model put forward is able to characterize particles for a broad range of distances to the focal plane with limited cross-correlation between the found *z*-position, and refractive index and diameter.

Here an approximate model for the aperture effect was put forward, limiting the fit to low scattering angles. Fitting of larger scattering angles would allow the user to garnish the full potential resolving power of the technique and also allow the use of larger aperture sizes to allow for more incident light.

The measured refractive index is lower than that found in literature. This can be due to either an effect which was not taken into account or because the particles actually have a lower refractive index. Since the method shows that the diameter is close to the diameter certified by the manufacturer, we tend to believe that the latter is true. More measurements with particles from different materials and with different sizes are needed to make hard conclusions, however.

The number of particles analyzed is rather low. Sufficient to demonstrate the method, but not enough to obtain statistical relevant data. In follow-up studies we plan to speed up the analysis workflow and test the method with different kinds of particles (different sizes and different materials). The current implementation still requires approximately 50 s for fitting of a single hologram, which is too slow to enable the analysis of a statistical relevant number of particles.

Other improvement routes could be to use an LED to obtain more light at the same coherence level and hereby increasing the resolving power.

Funding

This work was sponsored by Fonds voor Wetenschappelijk Onderzoek (FWO) (project G007513N).